Finite element simulations of aluminium plates under impact loading using a nano-scale material model

J. Johnsen[a], J. K. Holmen[a], O.R. Myhr[a,b], O.S. Hopperstad[a] and T. Børvik[a,c,*]

[a] *Structural Impact Laboratory (SIMLab), Centre for Research-based Innovation (CRI) and Department of Structural Engineering, Norwegian University of Science and Technology, NO-7491 Trondheim, Norway*

[b] *Hydro Aluminium, Research and Technology Development (RTD), NO-6601 Sunndalsøra, Norway*

[c] *Norwegian Defence Estates Agency, Research and Development Section, NO-0015 Oslo, Norway*

Abstract

Finite element simulations of AA6070 aluminium plates struck by ogival-nose projectiles are performed. The aluminium plates are 20 mm thick and heat treated to temper O, T4, T6 and T7. A nano-scale material model, consisting of three parts: a precipitation model, a yield-strength model and a work-hardening model, is used to predict the flow-stress curves of the materials at ambient temperature based on the chemical composition of the alloy and the thermal history defined by the heat treatment. Finite element simulations of the perforation process are then carried out using both 3D solid and 2D axisymmetric elements. The numerically-obtained ballistic limit velocities, predicted without any use of data from mechanical tests, are compared with available experimental data and found to be in excellent agreement with the experimental ones for all tempers. The same holds for the predicted residual velocities at striking velocities higher than the ballistic limit.

Keywords: Ballistic impact, AA6070, nano-scale model, numerical simulations, experimental validation

1. Introduction

Age-hardening aluminium alloys are attractive materials for application in lightweight protective structures owing to their high strength-to-weight ratio and good energy absorption capability [1]. The yield strength, work hardening and ductility of these alloys depend on the alloying elements and the heat treatment, but increased strength is usually gained at the expense of lower work hardening and ductility [2]. For a given structural application, it

* Corresponding author. Tel.: + 47-73-59-46-47; fax: + 47-73-59-47-01.

E-mail address: tore.borvik@ntnu.no (T. Børvik).

should then be possible, at least in principle, to find an optimal combination of strength, work hardening and ductility by carefully varying the chemical composition of the alloy and the heat treatment. However, if the material properties have to be determined through a number of mechanical tests, such an approach would be both time consuming and expensive.

Recently, nano-scale material models have been proposed that are capable of predicting with reasonable accuracy the strength [3][4] and work hardening [5][6] of certain classes of age-hardenable aluminium alloys as a function of the chemical composition and heat treatment. The basis for such modelling must be a precipitation model that is sufficiently relevant and comprehensive to deal with non-isothermal heat treatments in an adequate manner. This requires accurate predictions of the decomposition of a solid solution by the formation of a precipitate structure. The precipitation model applied in the present investigation is based on the previous works by Langer and Schwartz [7], Kampmann et al. [8] and Wagner and Kampmann [9] who treat nucleation, growth and coarsening as coupled processes within a framework that is suitable for numerical simulations. The further coupling between the predicted precipitate structure and the resulting yield strength at room temperature can be obtained from established dislocation theory, based on a consideration of the intrinsic resistance to dislocation motion due to solute atoms and particles, as described in numerous publications, see e.g. [10], [11] and [12].

The final prediction of the resulting work hardening based on a given precipitate structure has been considered by several authors, and the present modelling adopts the basic principles described by Ashby [13], where the total dislocation density is split into statistically stored and geometrically necessary dislocations. This allows a separate treatment of each category of dislocations, where the density of geometrically necessary dislocations can be evaluated from the characteristics of the precipitate structure (i.e. volume fraction and size). The density of the statistically stored dislocations depends on the balance between accumulation and annihilation of dislocations by dynamic recovery as described by Kocks [14] and Mecking and Kocks [15]. Cheng and co-workers [16] combined the basic principles of the Ashby and the Kocks models in order to calculate complete stress-strain curves for Al-Mg-Si alloys that were heat treated to different temper conditions. However, since a precipitation model was not included, this approach cannot be used to predict the resulting stress-strain curve from a given chemical composition and temperature history.

The objective of the current study is to evaluate the possibility of predicting the perforation process and the ballistic limit velocity of AA6070 plates struck by ogival-nose projectiles without using any data from mechanical tests. The nano-scale material model

NaMo (Nanostructure Model, see [5][6]) is used to determine the flow-stress curves of the materials based on the chemical composition of the alloy and the thermal history defined by the heat treatment. NaMo consists of three sub-models that are fully integrated in a computer code, i.e. a precipitation model, a yield-strength model and a work-hardening model. The flow-stress curves predicted by NaMo are then used in finite element simulations of the perforation process using both 3D solid and 2D axisymmetric elements.

The results obtained by this approach are validated against an experimental study reported in Holmen et al. [17] on the perforation of 20 mm AA6070 plates by 7.62 mm AP bullets. The plates were tested in tempers O (annealed), T4 (naturally aged), T6 (peak strength) and T7 (overaged) to study the influence of yield strength, work hardening and ductility on the ballistic limit. In addition to the impact tests, quasi-static tensile tests on these materials were carried out, and used here for the purpose of validating the accuracy of the NaMo simulations. In the impact tests, the dominating failure mode was cavity expansion (also known as ductile hole growth in ballistics) even though some fragmentation occurred, especially for tempers with high strength and low ductility. The fragmentation was most prominent at the highest impact velocities and assumed less important for the ballistic limit. An observation made in the experimental study was that the yield strength is a more important feature than local ductility in ballistic impact for the investigated combination of plate materials, bullet type and impact velocities. It is demonstrated in the following that the agreement between the numerical predictions of the ballistic limit velocities using the proposed approach and the results obtained experimentally is good. The study thus shows how it is now possible to conduct finite element simulations of impact-loaded aluminium structures with confidence without any use of data from mechanical tests.

The organization of this paper is as follows. In Section 2, a brief description of the aluminium alloy and the various heat treatments is provided. The theoretical background of the NaMo model is given in Section 3, while Sections 4 presents the results from the NaMo simulations. In Section 5, the finite element modelling is described, and the numerical results are summarized in Section 6. The validation of the proposed approach against available experimental data is presented in Section 7. The modelling assumptions are discussed in Section 8, whereas some conclusions are given in Section 9.

2. Materials

The 20 mm thick target plates of aluminium alloy AA6070 with chemical composition as given in Table 1 were produced by DC-casting and hot-rolling at Hydro Aluminium's research laboratory in Bonn, Germany. The plates were heat treated to tempers O (annealed), T4 (naturally aged), T6 (peak strength) and T7 (overaged) according to Table 2. The material was characterised by quasi-static tensile tests in different in-plane directions at ambient temperature to determine the yield strength, work hardening, tensile strain to failure and plastic anisotropy, see [17] for details. It was found that the anisotropy in strength and work hardening was negligible, while the tensile strain to failure varied considerably with direction. Typical true stress-strain curves for the 0°, 45° and 90° orientations with respect to the rolling direction are shown in Figure 1a) for the different tempers. The scatter between repeated tests was insignificant. Flow-stress curves in terms of the equivalent von Mises stress versus the equivalent plastic strain for the 0° orientation are shown in Figure 1b). These curves were determined from the experimentally-obtained true stress-strain curves in Figure 1a) using finite element simulations in combination with an optimisation tool [17]. It is evident from these figures that the different heat treatments lead to substantial differences in the stress-strain behaviour of the materials, and this will influence the impact resistance of the plates.

The AA6070 plates in different tempers were struck by APM2 bullets fired from a smooth-bore rifle at various impact velocities [17]. The bullet consisted of a brass jacket, lead filler and an ogive-nose, hardened steel core. More information regarding the bullet materials can be found in Børvik et al. [18].

3. Theoretical outline of NaMo

Figure 2 describes the components of the nano-scale material model NaMo which is a combined precipitation, yield strength and work hardening model for age-hardening aluminium alloys [5][6]. The present version is comprehensively verified and validated for 6xxx series aluminium alloys (see e.g. [4][5][6][19][20]), but the basic principles and the mathematical framework are expected to be applicable also for other alloy systems like 2xxx and 7xxx alloys. The three sub-models shown in Figure 2 are fully integrated in a computer code, where the outputs from the precipitation model are inputs to both the yield-strength model and the work-hardening model.

In order to run a simulation, the alloy composition and the temperature-time history must be specified, from which the complete room temperature flow curve is eventually calculated by the program. The first step of a simulation is to invoke the precipitation model that calculates the evolution of the hardening precipitates by nucleation, growth or dissolution and eventually coarsening [6][21]. A range of different particles may form in 6xxx alloys depending on the chemical composition and the heat treatment, but the ones that are of main interest here are the nanometre scale hardening particles consisting of Mg and Si (e.g. β'' and β' particles), as well as clusters and GP-zones, which may form at room temperature. Each of these classes or groups of particles is represented by a separate Particle Size Distribution (PSD) in the model, i.e. one PSD for β'' and β' particles and one for clusters and GP-zones [20]. The schematic diagram in Figure 2 illustrates a discrete PSD, where each column corresponds to a certain number density of particles within the specific size class.

When the PSD is calculated by the program, the essential precipitation parameters can be extracted and transferred to the yield-strength and work-hardening models, as illustrated in Figure 2. For the yield-strength model, a key parameter is the mean obstacle strength $\overline{F}$ between a gliding dislocation and the intercepting particles which is defined as

$$\overline{F} = \frac{\sum_i N_i F_i}{\sum_i N_i} \tag{1}$$

where N_i is the number density of particles that belongs to a given size class Δr_i, and F_i is the corresponding obstacle strength. For weak particles it is assumed that F_i is proportional to the particle radius as long as r_i is smaller than the critical radius r_c for the transition from shearing to bypassing of particles [3][4], i.e.

$$F_i = 2\beta G b^2 \left(\frac{r_i}{r_c} \right) \tag{2}$$

Here β is a constant close to 0.5, G is the shear modulus and b is the magnitude of the Burgers vector. Conversely, for strong (non-shearable) particles, characterised by $r_i > r_c$, the obstacle strength F_i is constant and independent of r_i according to the following expression

$$F_i = 2\beta G b^2 \tag{3}$$

As shown in Figure 2, the effective particle spacing l in the slip plane is required input to the yield-strength model, and this parameter can be expressed in terms of the mean particle radius $\bar{r}$, the particle number density $N_v = \sum_i N_i$, and the mean obstacle strength $\overline{F}$ as

$$l = \left(N_v \bar{r} \frac{\overline{F}}{\beta G b^2} \right)^{-1/2} \tag{4}$$

Finally, the yield-strength model requires that the solid solution concentrations are known in order to estimate the strength contribution from solid solution hardening. The solid solution concentration of an element C_j, where j may correspond to e.g. Mg, is obtained from the continuity equation as follows

$$C_j = C_0 - \left(C_p - C_j \right) \sum_i \tfrac{4}{3} \pi r_i^3 N_i \tag{5}$$

Here, C_0 is the initial concentration of element j in the alloy and C_p is the concentration of the element in the particle. C_j is also input to the work-hardening model, where the solute level affects the ease by which dislocations of opposite sign may annihilate during deformation by dynamic recovery. Generally, the dynamic recovery is retarded when the solute level is increased, and the overall effect of a mixture of elements in solid solution can be estimated as described in [5] and [6].

According to Figure 2, the work-hardening model requires that the so-called geometric slip distance $\lambda_{g,o}$ is known. This is a measure of how far the dislocations move before they are stored in the vicinity of the non-shearable particles that are dispersed within the matrix material. The parameter can be extracted from the PSD as follows

$$\lambda_{g,o} = \left(8 \sum_i r_i^2 N_i \right)^{-1} \quad \text{for} \quad r_i > r_c \tag{6}$$

Here N_i is the number of particles per unit volume within the size class r_i and r_c is the critical radius defined above. Since only non-shearable particles are capable of storing geometrically necessary dislocations, the work hardening model requires that the volume fraction of these particles is estimated from the PSD as follows

$$f_o = \sum_i \frac{4}{3}\pi r_i^3 N_i \quad \text{for} \quad r_i > r_c \tag{7}$$

When all the relevant parameters in Figure 2 are extracted from the PSD, the complete stress-strain curve at room temperature can be predicted, and the flow stress σ_f can be calculated as a function of the plastic strain ε_p by the following expression

$$\sigma_f = \sigma_y + \Delta\sigma_d \tag{8}$$

Here σ_y and $\Delta\sigma_d$ are the room temperature yield stress and the net contribution from dislocation hardening, respectively. The response equations, i.e. the equations connecting the precipitate parameters shown in Figure 2 to σ_y and $\Delta\sigma_d$, will be described in the following.

In the yield-strength model, the individual contributions to the overall macroscopic yield stress σ_y are given as

$$\sigma_y = \sigma_i + \sigma_p + \sigma_{ss} \tag{9}$$

Here σ_i corresponds to the intrinsic yield stress of pure aluminium, and σ_p is the precipitation hardening contribution given as

$$\sigma_p = \frac{M\overline{F}}{bl} \tag{10}$$

where $\overline{F}$ and l are given in Eq. (1) – (4) and M is the Taylor factor. In Eq. (9) the solid solution hardening contribution of the alloy σ_{ss} is calculated assuming that the contribution from each alloying element is additive

$$\sigma_{ss} = \sum_j k_j C_j^{2/3} \tag{11}$$

Here C_j is the concentration of a specific alloying element in solid solution as given from Eq. (5), and k_j is the corresponding scaling factor.

The microstructure based work-hardening model predicts the individual evolution of statistically stored and geometrically necessary dislocations, respectively, based on well-established evolution laws. The evolution of statistically stored dislocations is predicted as the balance between statistical storage and dynamic recovery of dislocations, while the generation of geometrically necessary dislocations during plastic deformation is assumed to be associated with non-shearable particles.

The work-hardening model is novel in the way it includes the precipitate structure through the fully integrated NaMo model, as shown in Figure 2. This means that any changes in the PSD during a heat treatment will be reflected by a corresponding change in the work-hardening response, as represented by the net contribution from dislocation hardening $\Delta\sigma_d$ expressed by the following response equation

$$\Delta\sigma_d = \alpha MGb\sqrt{\left(\frac{k_1}{k_2}\right)^2\left(1-\exp\left(-\frac{k_2\varepsilon_p}{2}\right)\right)^2 + \rho_{g,s}^{ref}\frac{\lambda_{g,o}^{ref}}{\lambda_{g,o}}\frac{\min\left(\varepsilon_p,\varepsilon_c\right)}{\varepsilon_c^{ref}}} \tag{12}$$

Here, index *ref* means a chosen reference alloy, α is a numerical constant, while k_1 is a model parameter, expressing the storing rate of statistically stored dislocations. The alloy dependent parameter k_2 expresses the rate of dynamic recovery of statistically stored dislocations during plastic deformation, and depends on the solid-solution concentrations. $\lambda_{g,o}$ and $\lambda_{g,o}^{ref}$ are geometric slip distances as defined in Eq. (6). The parameters ε_c and ε_c^{ref} are critical macroscopic strains defining the saturation values for storing of geometrically necessary dislocations, which corresponds to a dislocation density $\rho_{g,s}^{ref}$ for the reference alloy. The parameters in Eq. (12) that are assumed to be invariable for 6xxx alloys are given in Table 3. The remaining three quantities in Eq. (12) that must be defined to obtain a unique description of the stress-strain curve are $\lambda_{g,o}$, k_2 and ε_c. The former variable is directly obtained from the PSD through Eq. (6), while the two latter parameters, i.e. k_2 and ε_c,

depend upon the equivalent Mg concentration of the alloy, $\hat{C}_{Mg}$, and the volume fraction of non-shearable particles, f_o, respectively, through the following relations

$$k_2 = k_1 \frac{\alpha MGb}{k_3 \left(\hat{C}_{Mg}\right)^{3/4}} \tag{13}$$

$$\varepsilon_c = \frac{f_o^{ref}}{f_o} \varepsilon_c^{ref} \tag{14}$$

In Eq. (13), k_3 is a material constant given in Table 3, while $\hat{C}_{Mg}$ can be approximated from the solid solution concentrations of Mg and Si as follows [5][6]: $\hat{C}_{Mg} = C_{Mg} + 0.5C_{Si}$. The constants ε_c^{ref} and f_o^{ref} in Eq. (14) are defined in Table 3.

4. NaMo simulation results

The results presented in this section have been obtained without any calibration or tuning of the material constants and rely solely on the chemical composition and thermal history as defined by the temper condition as the only inputs.

Calculated PSDs for the four different temper conditions are shown in Figure 3a) and reveal significant differences. The critical radius r_c for transition from shearing to bypassing of particles by the dislocations is superimposed in the diagram. For the T4-condition the predicted PSD is narrow with a mean radius slightly larger than 10Å (i.e. 10^{-9} m). The particles are clusters or GP-zones and they are shearable by dislocations, since they are smaller than r_c. This is in contrast to the O-temper condition, where the majority of particles are Orowan particles, which means that they are larger than r_c and capable of generating geometrically necessary dislocations during deformation. Temper T6 and T7 contain a mixture of shearable and non-shearable particles, since r_c is located within their distributions.

The volume fractions of Orowan particles f_o are shown in Figure 3b), which reveals that f_o is significantly larger for the temper O and T7 conditions, compared with the T4 and T6 conditions. This is because growth and coarsening of the precipitates are enhanced by ageing

at high temperatures and long ageing times. Since the growth of particles is extremely slow at room temperature, $f_o = 0$ for the T4 temper, for which the particles are all smaller than r_c as shown in Figure 3a).

Figure 3c) shows the geometric slip distance $\lambda_{g,o}$ extracted from the different PSDs in Figure 3a) by using Eq. (6). It is interesting to note that the T7-temper gives the smallest $\lambda_{g,o}$ even though f_o is larger for the O-temper, as shown in Figure 3b). This is because the number density of particles is very low for the O-temper where the coarsening of particles has been severe during the heat treatment at a relatively high temperature, i.e. $350°C$. Note also that $\lambda_{g,o}$ is many decades higher for T4 than for the other tempers, and is therefore not shown.

The equivalent Mg concentration $\hat{C}_{Mg}$ for each temper condition is shown in Figure 3d). The T4-temper material contains clusters or GP-zones, which tie up just a modest amount of solute due to their small size. Hence, a major fraction of solute remains in solid solution at the end of the room temperature storing, and $\hat{C}_{Mg}$ is therefore relatively large for the T4-alloy. For the other three conditions, i.e. T6, T7 and O, most of the solute available at the start of the ageing process has been consumed as a consequence of precipitation reactions taking place during the ageing heat treatments, which leads to a low $\hat{C}_{Mg}$ concentration for all these tempers, as shown in Figure 3d).

Flow-stress curves as predicted by NaMo for all tempers are shown in Figure 4a), where they are compared to corresponding curves based on the experimental tests. The general impression is that the agreement between simulations and measurements is reasonably good when taking into consideration that no calibration or tuning has been done. The main discrepancies are the overestimation of the yield strength as well as the underestimation of the work-hardening rate for some of the tempers, but the main trends seem to be well captured. This is better outlined in Figure 4b), where the same curves are plotted in the range $\varepsilon_p \in [0; 0.25]$. Even though the flow-stress curves for temper T6 and T7 do not coincide with the experimental ones, the work-hardening is very similar. The underestimation of the work-hardening rate at large strains by NaMo, which is sometimes observed, is caused by the fact that at present NaMo does not include stage IV work hardening.

5. Finite element modelling

5.1. Constitutive relation

The materials are assumed to be isotropic and the J_2 flow theory is used to model the elastic-plastic material behaviour (see e.g. [22]), i.e. the von Mises yield criterion, the associated flow rule and isotropic hardening are adopted in the simulations. The yield criterion is expressed as

$$f = \sigma_{eq}(\boldsymbol{\sigma}) - \sigma_f(\varepsilon_p) = 0 \tag{15}$$

where $\boldsymbol{\sigma}$ is the Cauchy stress tensor, and σ_f is the flow stress defined by NaMo, as described in Section 3. The equivalent stress is defined by

$$\sigma_{eq}(\boldsymbol{\sigma}) = \sqrt{\tfrac{3}{2}\mathbf{s}:\mathbf{s}} \tag{16}$$

where $\mathbf{s} = \boldsymbol{\sigma} - \frac{1}{3}(\mathrm{tr}\,\boldsymbol{\sigma})\mathbf{I}$ is the deviatoric stress tensor and $\mathbf{I}$ is the 2nd-order identity tensor. The plastic strain ε_p is taken to be the equivalent plastic strain associated with the von Mises yield criterion, i.e.

$$\varepsilon_p = \int_0^t \dot{\varepsilon}_p dt, \quad \dot{\varepsilon}_p = \sqrt{\tfrac{2}{3}\mathbf{D}^p:\mathbf{D}^p} \tag{17}$$

where $\mathbf{D}^p$ is the plastic rate-of-deformation tensor defined by the associated flow rule. The elastic behaviour is determined by Young's modulus E and Poisson's ratio ν. The flow-stress curves predicted by NaMo (see Figure 4), using the constants compiled in Table 3, were applied in the finite element simulations. Table 4 gives the required physical constants for all tempers. In a similar way as in analytical calculations using the cavity expansion theory, see e.g. [23][24][25], any strain-rate and temperature dependence of the material response is neglected in the numerical simulations. The constitutive relation and parameters for the bullet material were taken from Børvik et al. [18].

5.2. Finite element models

Finite element simulations of the perforation process were carried out using both 3D solid and 2D axisymmetric elements, and tiny pinholes in the plates were used to avoid the need for a fracture criterion. For 3D conditions, the explicit finite element code IMPETUS Afea Solver [26] was used for the simulations. The bullet and the region in the target plate that undergoes large plastic deformations were modelled using fully integrated 3rd-order 64-node hexahedrons. The geometry of the target was similar to that used in the tests, except that it was modelled circular and somewhat smaller than the real size to save CPU time. The influence of using a target of reduced size in the simulations was studied in [17] and found to be negligible. The simulations were done with only the rigid, hard steel core instead of the full bullet, which significantly reduced the computational time. It has been shown experimentally in e.g. [24] and [25] that the brass jacket and the lead filler have a relatively small effect on the perforation process of monolithic 20 mm thick aluminium plates. The symmetry in the model was exploited by modelling only ⅛ of the bullet and the target plate. Outside the impact region 20 fully integrated linear elements were used over the thickness of the plate, giving a node spacing of 1 mm in all directions, while 20 cubic 3rd-order 64-node elements were used over the thickness in the impact region. This gave a node spacing of 0.33 mm in all directions in the critical region, and consequently 60 nodes over the thickness of the plate.

A plot of the finite element mesh used in the 3D simulations is shown in Figure 5a). A mesh convergence study was performed in [17], and it was found that the solution had converged in terms of the ballistic limit velocity when 20 higher-order elements (giving 60 nodes) were used over the target thickness. A pinhole was introduced in the centre of the plate with a radius of 0.1 mm (see also Figure 6). Since the major failure mode was cavity expansion, this seems to be a reasonable approach. It has been shown in previous studies that the influence of the pinhole on the penetration process is minor [23]. Contact between the various parts was established using a penalty-based node-to-surface contact algorithm without friction available in the IMPETUS Afea Solver. In the current work, all exterior nodes and element faces were active in the contact.

For 2D axisymmetric conditions, a similar model as described above was established in the explicit finite element code LS-DYNA [27]. Here, the mesh consisted of 4-node axisymmetric elements with one integration point and stiffness-based hourglass control. Contact between the various parts was modelled using an automatic 2D penalty formulation without friction. A fixed mesh with an element size of $0.33 \times 0.33\,\mathrm{mm}^2$ was chosen in the

target. This gave a total of 60 elements over the target thickness, i.e. node spacing identical to that used in the solid element model. A plot of the 2D finite element mesh used in the simulations is shown in Figure 5b). Also in this model a pinhole was introduced in the centre of the plate with a radius of 0.1 mm (see also Figure 7).

6. Numerical results

Typical plots of the perforation process for temper T4 at an initial velocity just above the ballistic limit as predicted by the IMPETUS Afea Solver are given in Figure 6, where the fringes represent the equivalent plastic strain field. Similar plots of the perforation process for temper T6 as predicted by LS-DYNA are given in Figure 7. The pinholes in the models are easily recognised, and both the 3D solid and the 2D axisymmetric models seem to capture the penetration and perforation process by cavity expansion very well.

From each simulation using the models presented above, initial (v_i) and residual (v_r) velocities of the bullet were recorded. Based on extensive series of numerical simulations, the initial versus residual velocity curve and the ballistic limit velocity for each temper of AA6070 were established. The results are plotted in Figure 8 (IMPETUS simulations) and in Figure 9 (LS-DYNA simulations), where they are compared with the experimental data from Holmen et al. (2012). A modified version of the Recht-Ipson model [28], also known as the Lambert-Jonas equation [29], was used to determine the trend-lines through the data points as

$$v_r = a\left(v_i^p - v_{bl}^p\right)^{1/p} \tag{18}$$

Here $a = 1$ and $p = 2$ are analytical constants taken from [28], while v_{bl} is the ballistic limit velocity that was fitted to the numerical results. The main results are also compiled in Table 5, and a monotonic and rather linear increase in ballistic limit velocity with target yield strength is found. Similar results have been obtained for steel targets [18].

7. Experimental validation

The numerical results based on the flow-stress curves from NaMo were validated against experimental results previously published by Holmen et al. [17]. In the experimental tests, the

AA6070 plates were struck by APM2 bullets at various impact velocities. The bullets have 7.62 mm diameter, 10.5 ± 0.25 g mass, and consists of a brass jacket, lead filler and a 5 ± 0.25 g, ogive-nose, hardened steel core with a calibre-radius-head of 3 and a Rockwell C hardness of 63. The impact tests were carried out in a compressed gas-gun facility described in [30], using a specially designed smooth-bored Mauser rifle with a barrel length of about 1 m to fire the bullets. Square, 20 mm thick AA6070 plates of in-plane dimensions 300×300 mm^2 were tightly clamped to a rigid frame by two beams inside an impact chamber, thus providing a fixed boundary for the horizontal sides of the targets, while the vertical sides remained free. The in-plane distance between each impact point and the target boundary was roughly 100 mm. Impact and residual velocities were measured with various optical devices [18], whereas the overall perforation process was captured with a high-speed video camera. By adjusting the ammunition, impact velocities in a range from just below to well above the ballistic limit were obtained. Between six and nine tests were conducted for each temper to determine the ballistic limit velocity with sufficient accuracy. Some high-speed video images of the perforation process of AA6070 plates in different tempers at impact velocities relatively close to the respective ballistic limits are shown in Figure 10. The amount of fragmentation from the targets at these impact velocities is small.

The experimental test data are compared with the numerical results in Figure 8 and Figure 9 in terms of residual versus initial velocity curves, while the predicted and experimentally-obtained ballistic limit velocities are given in Table 5. The numerical results are as seen conservative, i.e. the ballistic limit velocities are somewhat under-estimated for all tempers. However, the maximum deviation in ballistic limit velocity compared with the experimental data is less than 10%, independent of temper and numerical technique. The largest deviation is found for temper O, while the agreement between the experimental and numerical data for temper T7 is excellent. It should also be noted that the difference in results using 2D axisymmetric elements in LS-DYNA and 3D higher-order solids in IMPETUS is negligible.

8. Discussion

To be able to run numerical simulations of the ballistic impact problem without any use of data from mechanical tests, several assumptions are required. In the following the accuracy of the numerical predictions in terms of the ballistic limit velocity is discussed in some detail.

As already pointed out, NaMo seems to overestimate the yield stress and underestimate the work-hardening at large plastic strains. It is thus difficult to state to what extent this will affect the predicted response. However, it has been shown both experimentally and numerically that the target strength is the single most important parameter affecting the ballistic limit velocity during structural impact, and the data indicates a linear increase in perforation resistance with target yield stress [17][18]. The observation that NaMo overestimates the yield stress should therefore give non-conservative results, whereas the underestimation of the work hardening for large strains should contribute to more conservative predictions.

The influence of temperature and strain rate on the flow stress has been neglected in the numerical simulations. The reason for this is that NaMo provides the flow-stress curve at room temperature and at quasi-static strain rates. The neglect of the former will give non-conservative results, while the neglect of the latter will give conservative results. However, the rate sensitivity of 6xxx aluminium alloys is usually found to be small at room temperature. Experimental studies indicate an increase by about 10–15% or less from quasi-static loading conditions to a strain rate in the order of 10^3 s^{-1} [31][32]. At elevated temperature, however, the rate sensitivity is assumed to be stronger. Also the temperature sensitivity of 6xxx alloys is strong. As an example, Ostercamp et al. [31] found that depending of the strain rate AA6082-T6 has left only 20–30% of its strength at $20°C$ when the temperature is raised to $375°C$. Numerical simulations assuming adiabatic conditions confirmed that it is only the element row closest to the penetrating projectile that reaches such temperatures, and the temperature field is rapidly approaching the room temperature. The effect of assuming adiabatic versus isothermal conditions on the ballistic limit velocity in numerical simulations of aluminium plates struck by pointed-nose projectiles is thus moderate, as also confirmed in [23]. The heat transfer was further studied by conducting coupled thermal and structural simulations. No significant difference in the local temperature increase was obtained between simulations allowing heat conduction and those assuming adiabatic conditions. Since the temperature dependence seems to be the most significant, neglecting both the strain-rate and the temperature sensitivities is assumed to give non-conservative predictions of the ballistic capacity of these materials.

To simplify the finite element models and to save CPU time, only the hard steel core of the full APM2 bullet was modelled. Even though the mass of the brass jacket and the lead filler represents 50% of the total mass of the bullet, it has been shown experimentally that these parts only have a small effect on the perforation process (see e.g. [24][25]), since they

will be ripped off the penetrating core immediately after impact. However, the general trend from these experimental studies is that the ballistic limit velocity will drop by a few percentages when the full bullet is fired. Thus, neglecting these parts in the finite element models will give non-conservative results.

To predict fracture in ballistic impact may be a challenging task (see e.g. [33][34]). In this study, a tiny pinhole was introduced in the centre of the plate to avoid the need for a fracture criterion. Pinholes are motivated by the presumption that the projectile trajectory during perforation is known a priori. The effect of using a pinhole in finite element simulations has been studied by e.g. Chen [35] and Camacho and Ortiz [36], and little or no effect on the results of the calculations was found. This was also checked in this study, and simulations with pinholes in the range from 0.1 mm to 0.3 mm were run in LS-DYNA. No notable effect on the residual velocity of the bullet after perforation was registered. Chen [35] further stated that a pinhole is the numerical equivalent to cavity expansion theory, where an initial hole of infinitesimal size is assumed. The cavity expansion theory was first proposed by Bishop et al. [37] and further developed by Forrestal and co-authors (see e.g. [38]). However, the introduction of weak zones like a pinhole in the target plate should cause conservative results.

Frictional effects are frequently neglected in impact problems due to their unknown nature. According to Ravid and Bodner [39], a dynamic friction coefficient of 0.1 is proposed in the literature for metal working operations. They proposed to use a lower value of 0.05 for the lateral surfaces in impact situations due to the higher velocities and temperatures. In Zukas et al. [40], a dynamic friction coefficient of 0.01 is suggested for ballistic impact involving metal to metal surfaces. However, since friction in the sliding contact is neglected in these simulations, this should contribute to conservative results.

Finally, a number of studies (see e.g. [23][41]) have shown that the mesh-size sensitivity in numerical simulations of ballistic impact by pointed-nose projectiles (causing failure by cavity expansion) is much less than in corresponding simulations using blunt-nose projectiles (causing failure by adiabatic shear banding). However, it is expected that the numerical results will converge “from above”, meaning that the ballistic limit will drop somewhat with refined meshes. This effect will give non-conservative predictions.

The end outcome in this study is that the numerical simulations consistently give conservative results (see Table 5), which of course is desirable from a designer’s point of view. However, the reason for this is not readily explained, since the influence of the various

assumptions go both ways. It is further believed that this is at least to some extent problem dependent and may change according to the problem at hand.

9. Conclusions

A nano-scale material model (NaMo) has been used to determine the yield stress and the flow-stress curves of the aluminium alloy AA6070 in four different tempers (O, T4, T6 and T7). Only the chemical composition of the alloy and the temperature-time histories are required inputs for NaMo analyses. The flow-stress curves predicted with NaMo were used in numerical simulations in combination with the J_2 flow theory, while a pinhole in the target was used to avoid introducing a fracture criterion. Finite element simulations (using both 3D solid and 2D axisymmetric elements) of 20 mm thick plates struck by ogival-nose projectiles were performed and compared with available experimental data. The numerically obtained ballistic limit velocities and curves, predicted without any data from mechanical tests, are found to be in excellent agreement with the experimental results for all tempers (with a maximum deviation of less than 10%). Thus, the study suggests that NaMo is well suited for computer-aided design of aluminium structures, since it makes it possible to evaluate several alloys and tempers for the structural application at hand without performing costly materials tests.

Acknowledgement

The financial support of this work from the Structural Impact Laboratory (SIMLab), Centre for Research-based Innovation (CRI) at the Norwegian University of Science and Technology, is gratefully acknowledged.

References

[1] J.E. Hatch, Aluminium: Properties and Physical Metallurgy. American Society for Metals, Metals Park, Ohio (1984).

[2] D.J. Lloyd, Scripta Materialia 48 (2003) 341-344.

[3] A. Deschamps, Y. Brechet, Acta Materialia 47 (1999) 293-305.

[4] O.R. Myhr, Ø. Grong, S.J. Andersen, Acta Materialia 49 (2001) 65-75.

[5] O.R. Myhr, Ø. Grong, K.P. Pedersen, Metallurgical and Materials Transactions 41A (2010) 2276-2289.

[6] O.R. Myhr, Ø. Grong, ASM Handbook, Welding Fundamentals and Processes, Modeling of Metallurgical Microstructure Evolution in Fusion Welding. T. Lienert, T. Siewert, S. Babu, V. Acoff (Editors), 797-818 (2011).

[7] J.S. Langer, A.J. Schwartz, Physical Review A 21 (1980) 948-958.

[8] R. Kampmann, H. Eckerlebe, R. Wagner, Materials Research Society Symposia Proceedings 57 (1987) 526-542.

[9] R. Wagner, R. Kampmann, Materials Science and Technolgy - A Comprehensive Treatment, Vol. 5, 213-303, VCH Verlag, Weinheim, Germany (1991).

[10] J. Friedel, Dislocations, Pergamon Press, Oxford, UK (1964).

[11] F.R.N. Nabarro, Theory of Crystal Dislocations, Oxford University Press, UK (1967).

[12] B. Reppich, Material Science and Technology - A Comprehensive Treatment. R.W. Chan, P. Haasen, E.J. Kramer (Editors), Vol. 6, 315-326, VCH Verlag, Weinheim, Germany (1993).

[13] M.F. Ashby, Philosophical Magazine 21 (1970) 399-424.

[14] U.F. Kocks, Journal of Engineering Materials and Technology 98 (1976) 76-85.

[15] H. Mecking, U.F. Kocks, Acta Metallurgica 29 (1981) 1865-1875.

[16] L.M. Cheng, W.J. Poole, J.D. Embury, D.J. Lloyd, Metallurgical and Materials Transactions A 34 (2003) 2473–2481.

[17] J.K. Holmen, J. Johnsen, S. Jupp, O.S. Hopperstad, T. Børvik, International Journal of Impact Engineering (10.1016/j.ijimpeng 10.1016/j.ijimpeng.2013.02.002.2013.02.002).

[18] T. Børvik, S. Dey, A.H. Clausen, International Journal of Impact Engineering 36 (2009) 948-964.

[19] O.R. Myhr, Ø. Grong, H.G. Fjær, C.D. Marioara, Acta Materialia 52 (2004) 4997-5008.

[20] C. Schäfer, O.R. Myhr, Z. Liang, H.J. Brinkman, O. Engler, J. Hirsch, C. Chang, J. Banhart, Proceedings of the 13th International Conference on Aluminium Alloys (ICAA 13), June 3-7, Pittsburgh, PA, USA (2012).

[21] O.R. Myhr, Ø. Grong, Acta Materialia 48 (2000) 1605-1615.

[22] T. Belytschko, W.K. Liu, B. Moran, Nonlinear finite elements for continua and structures. John Wiley & Sons, Ltd., New York (2000).

[23] T. Børvik, M.J. Forrestal, O.S. Hopperstad, T. Warren, M. Langseth, International Journal of Impact Engineering 36 (2009) 426-437.

[24] T. Børvik, M.J. Forrestal, T.L. Warren, Experimental Mechanics 50 (2010) 969-978.

[25] M.J. Forrestal, T. Børvik, T.L. Warren, Experimental Mechanics 50 (2010) 1245-1251.

[26] IMPETUS Afea Solver, www.impetus.no [cited: 20.09.2012].

[27] LSTC, LS-DYNA Keyword User's Manual, Version 971. Livermore Software Technology Corporation, CA (2007).

[28] R.F. Recht, T.W. Ipson, Journal of Applied Mechanics 30 (1963) 384-390.

[29] J.A. Zukas, Impact Dynamics. Krieger Publishing Company, Florida (1992).

[30] T. Børvik, M. Langseth, O.S. Hopperstad, K.A. Malo, International Journal of Impact Engineering 22 (1999) 855–87.

[31] L.D. Oosterkamp, A. Ivankovic, G. Venizelos, Material Science and Engineering A278 (2000) 225-235.

[32] Y. Chen, A.H. Clausen, O.S. Hopperstad, M. Langseth, International Journal of Solids and Structures 46 (2009) 3825-3835.

[33] S. Dey, T. Børvik, O.S. Hopperstad, M. Langseth, Computational Materials Science 38 (2006) 176-191.

[34] E.A. Flores-Johnson, O. Muránsky, C.J. Hamelin, P.J. Bendeich, L. Edwards, Computational Materials Science 58 (2012) 131-139.

[35] E.P Chen, Mechanics of Materials 10 (1990) 107-15.

[36] G.T. Camacho, M. Ortiz, Computer Methods in Applied Engineering 42 (1997) 269-301.

[37] R.F. Bishop, R. Hill, N.F. Mott, Proceedings of the Royal Society 57 (1945) 147-159.

[38] M.J. Forrestal, T.L. Warren, International Journal of Impact Engineering 36 (2009) 220-225.

[39] M. Ravid, S.R. Bodner, International Journal of Engineering Sciences 21 (1983) 577-591.

[40] J.A. Zukas, High Velocity Impact Dynamics. John Wiley & Sons, New York (1990)

[41] T. Børvik, O.S. Hopperstad, K.O. Pedersen, International Journal of Impact Engineering 37 (2010) 537-551.

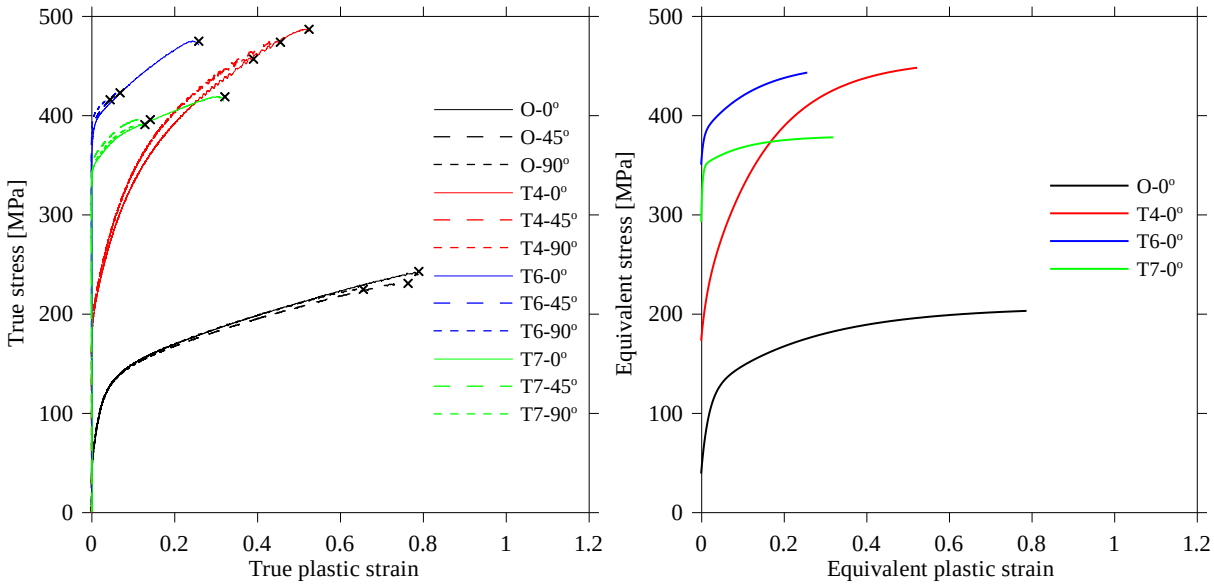

(a) (b)

Figure 1. a) Typical true stress-plastic strain curves for the 0°, 45° and 90° orientations with respect to the rolling direction of all tempers (where the black crosses indicate the fracture strain) and b) corresponding flow-stress curves for the 0° direction based on inverse modelling using LS-OPT (from [17]).

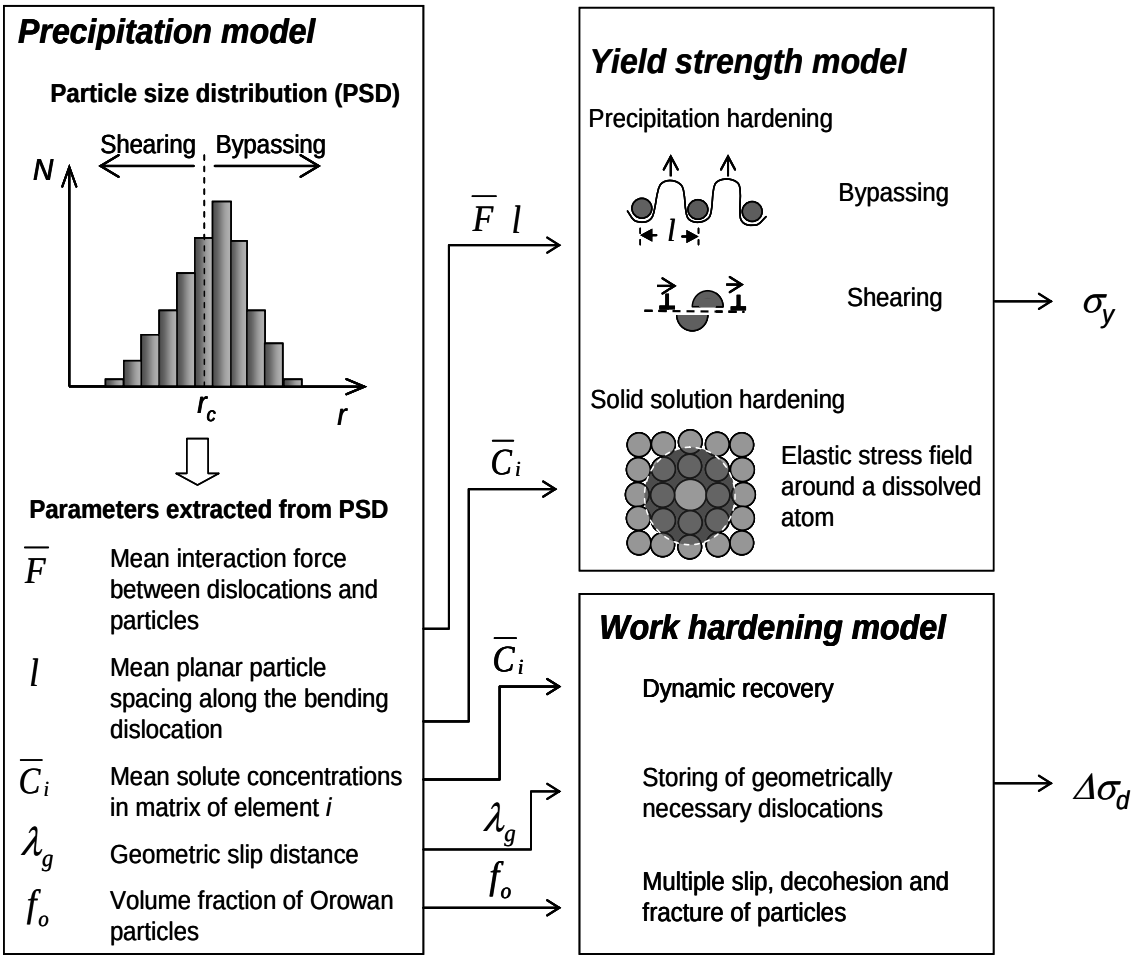

Figure 2. Diagram defining the parameters extracted from the Particle Size Distribution (PSD) and transferred to the yield-strength and work-hardening models.

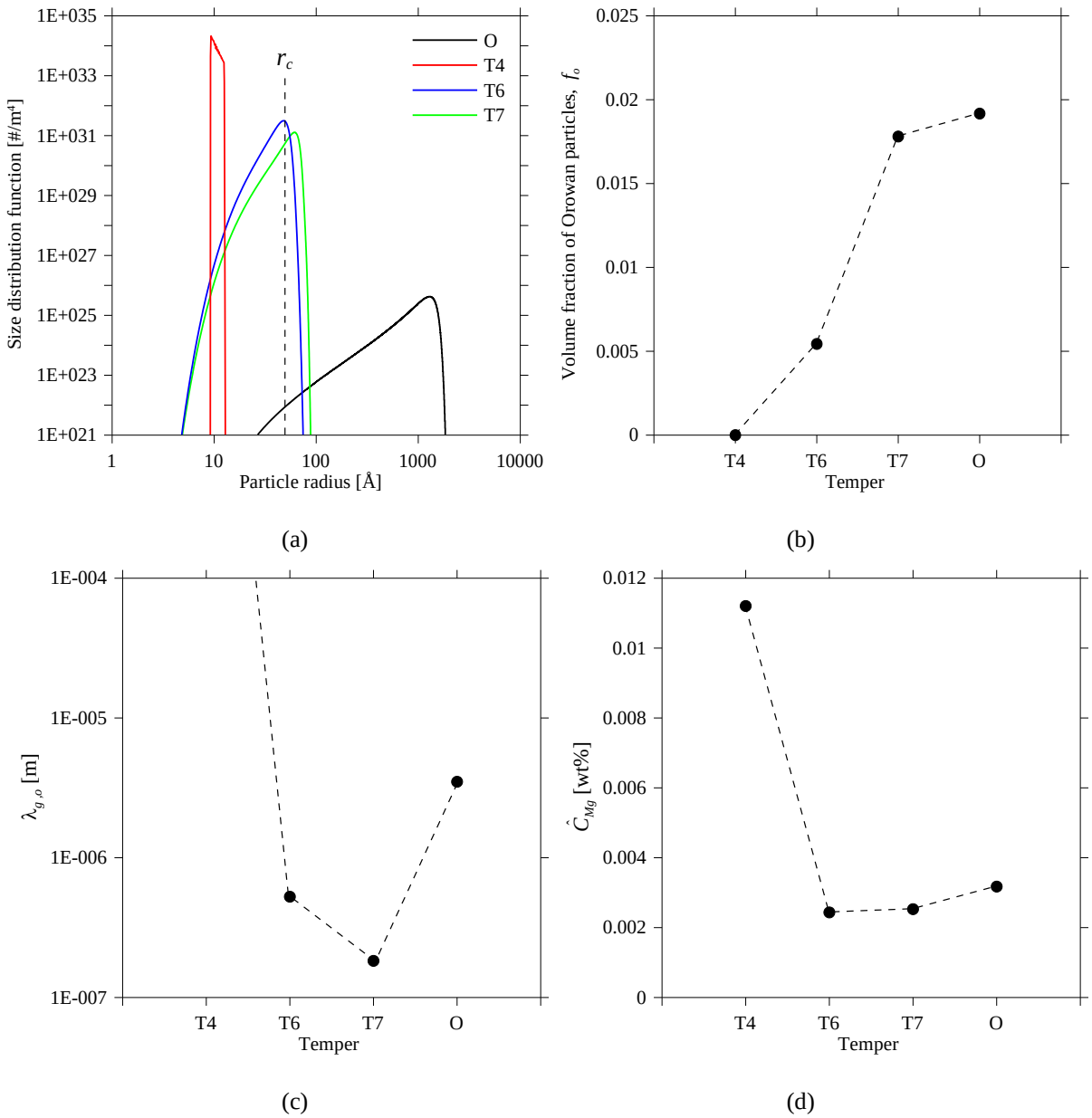

Figure 3. Some predictions by the NaMo model: a) Particle size distribution, b) volume fraction of Orowan particles, c) geometric slip distance and d) equivalent concentration of Mg in the various tempers.

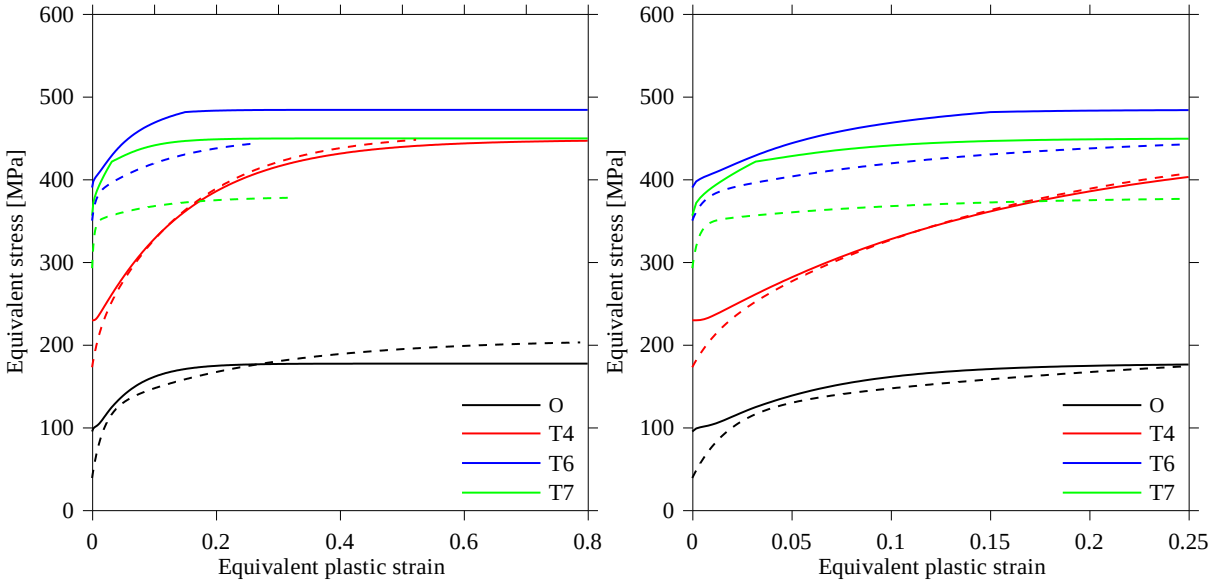

(a) (b)

Figure 4. a) Flow-stress curves for all tempers, defined in terms of the equivalent stress and the equivalent plastic strain according to the von Mises yield criterion in the range $\varepsilon_p \in [0;0.8]$, and b) corresponding curves as in a) in the range $\varepsilon_p \in [0;0.25]$. The solid lines are predictions obtained with NaMo, while the dashed lines are corresponding curves from the experiments.

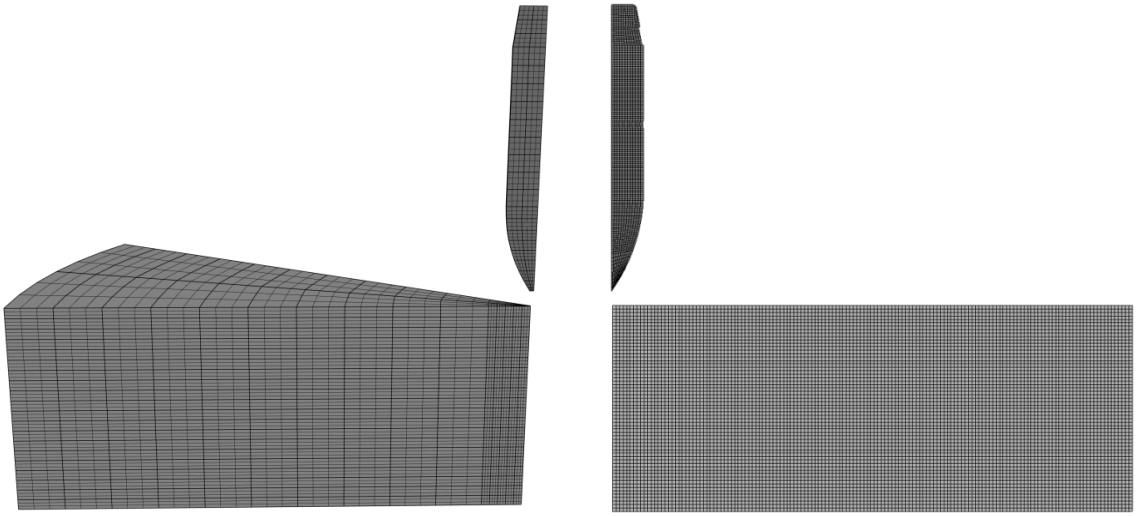

(a) (b)

Figure 5. a) Solid element mesh used in the IMPETUS Afea Solver simulations, where only ⅛ of the projectile and target plate is modelled due to the rotational symmetry of the problem, and b) 2D axisymmetric element mesh used in the LS-DYNA simulations. The radius of the pinhole in both meshes is 0.1 mm.

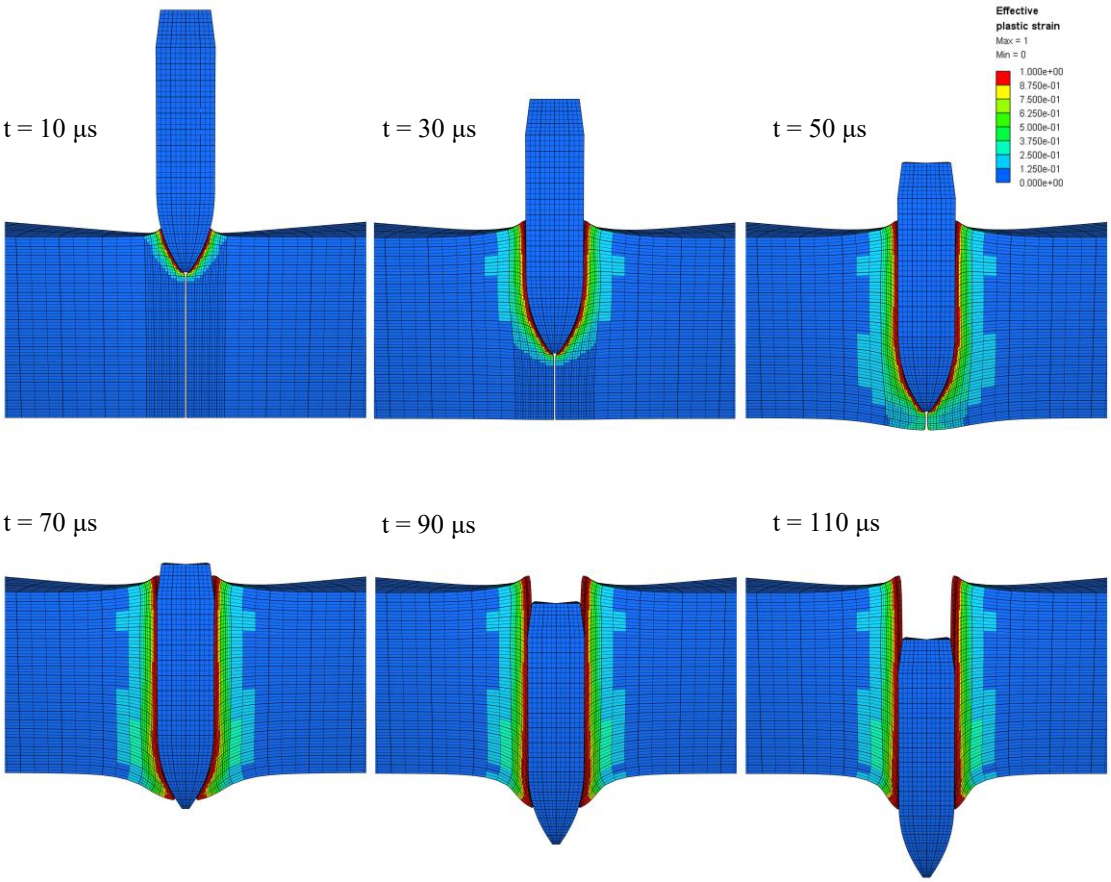

Figure 6. Perforation of a 20 mm thick AA6070 plate in temper T4 by the hard core of the APM2 bullet ($v_i = 503$ m/s, $v_r = 180$ m/s) as predicted by the IMPETUS Afea Solver. The fringes represent the equivalent plastic strain field in the range 0 to 1, and the solid model has been reflected about the centreline to better illustrate the pinhole.

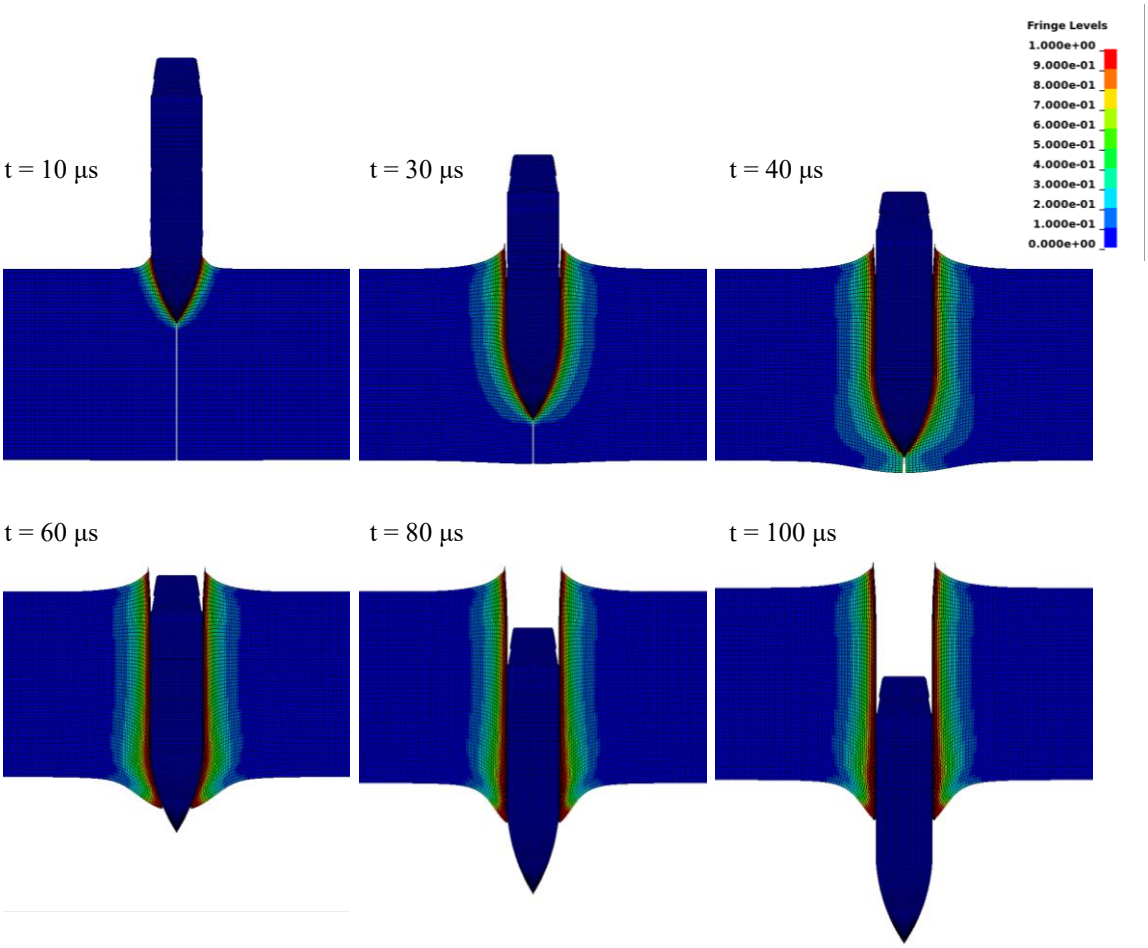

Figure 7. Perforation of 20 mm thick AA6070 plate in temper T6 by the hard core of the APM2 bullet ($v_i = 600$ m/s, $v_r = 271$ m/s) as predicted by LS-DYNA. The fringes represent the equivalent plastic strain field in the range 0 to 1, and the 2D axisymmetric model has been reflected about the centreline to better illustrate the pinhole.

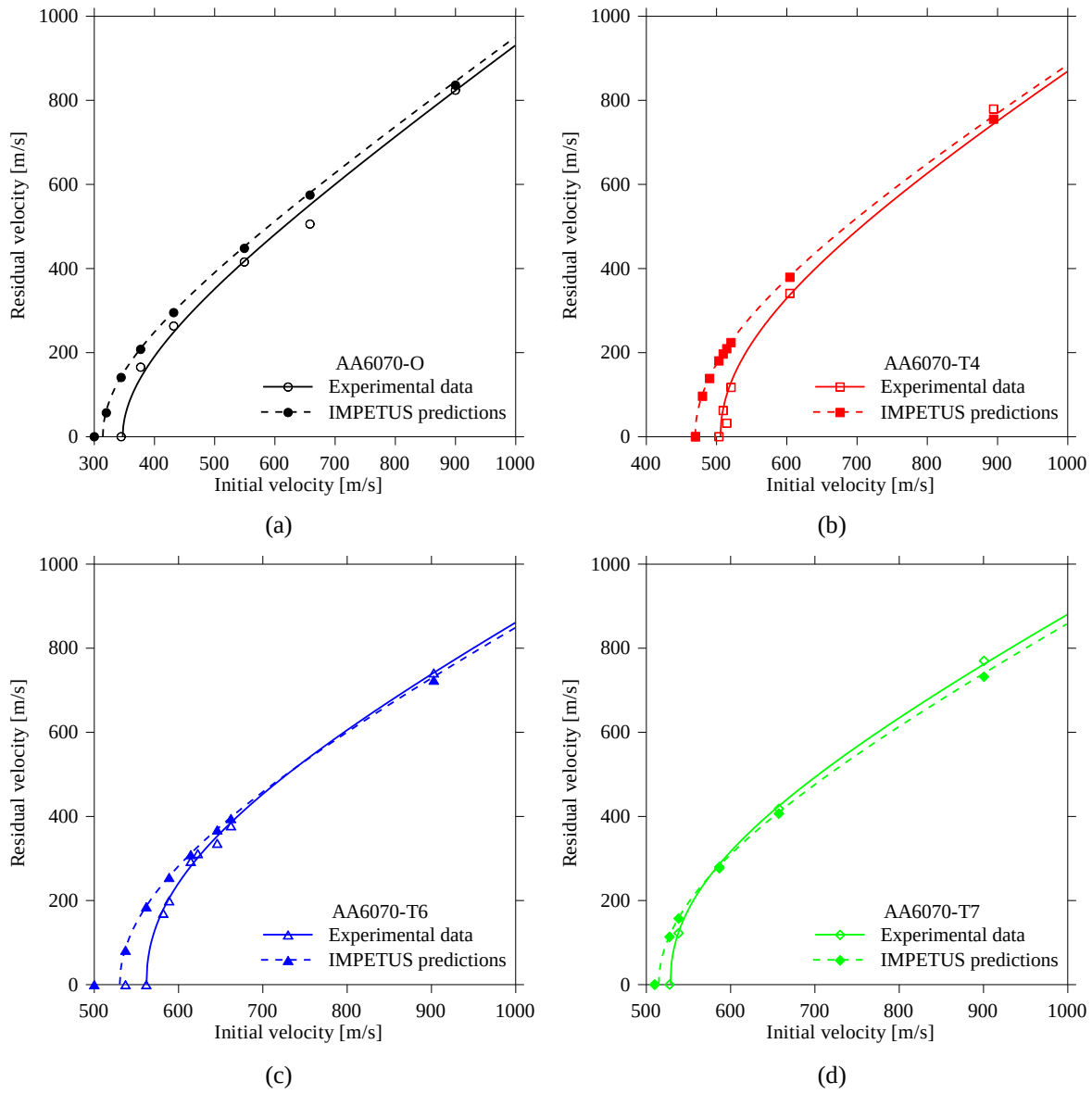

Figure 8. Residual versus initial velocity curves for a) AA6070-O, b) AA6070-T4, c) AA6070-T6 and d) AA6070-T7 from the IMPETUS Afea Solver simulations compared to the experimental results.

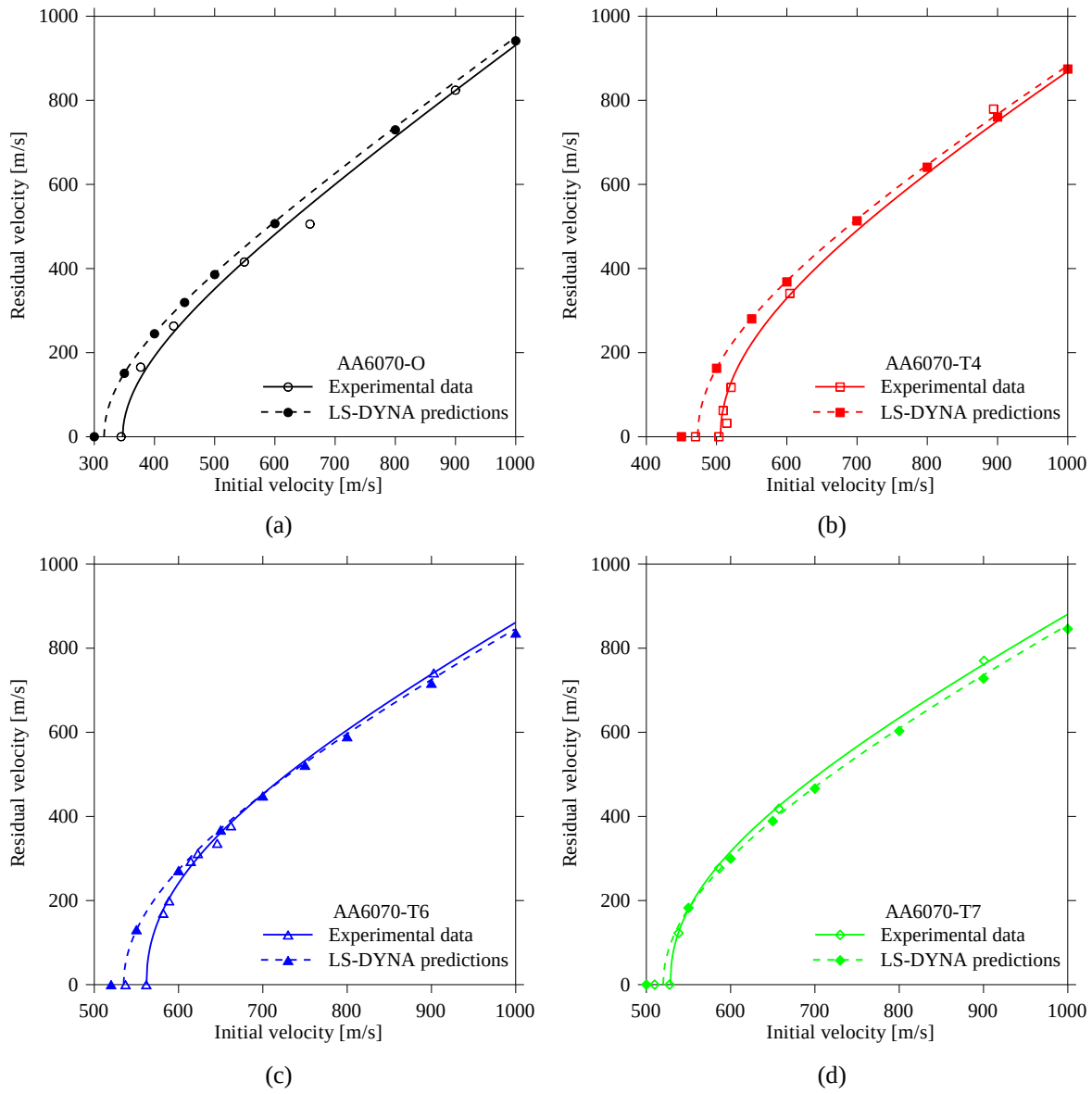

Figure 9. Residual versus initial velocity curves for a) AA6070-O, b) AA6070-T4, c) AA6070-T6 and d) AA6070-T7 from the LS-DYNA simulations compared to the experimental results.

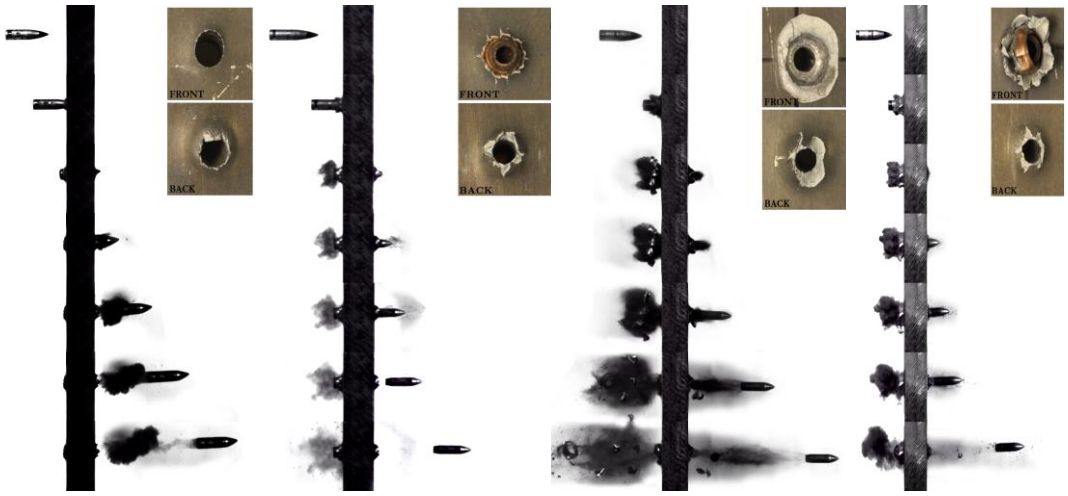

(a) (b) (c) (d)

Figure 10. Some high-speed video images showing the perforation process of a 20 mm thick AA6070 plate in temper a) O ($v_i = 377$ m/s, $v_r = 165$ m/s), b) T4 ($v_i = 509$ m/s, $v_r = 62$ m/s), c) T6 ($v_i = 615$ m/s, $v_r = 293$ m/s) and d) T7 ($v_i = 538$ m/s, $v_r = 122$ m/s) at impact velocities relatively close to the respective ballistic limit.

Table 1. Chemical composition (in weight %) of aluminium alloy AA6070.

Al	Si	Fe	Cu	Mn	Mg	Others
Balance	1.38	0.22	0.26	0.54	1.23	0.15

Table 2. Heat treatment processes of AA6070 to obtain the different tempers.

Temper	Solutionizing	Cooling	Annealing/artificial aging	Cooling
O	90 min at 560 °C	Water quench	24 h at 350 °C	Slow cooling
T4	90 min at 560 °C	Water quench	-	-
T6	90 min at 560 °C	Water quench	64 h at 160 °C	Slow cooling
T7	90 min at 560 °C	Water quench	8 h at 200 °C	Slow cooling

Table 3. Summary of input parameters used in NaMo [5].

α	b (m)	G (N/m^2)	M	k_1	k_3 (N/m^{2}wt%$^{3/4}$)	$\lambda_{g,o}^{ref}$ (m)	f_o^{ref}	r_c (m)	$\rho_{g,s}^{ref}$ (m^{-2})	ε_c^{ref}
0.30	$2.84\cdot10^{-10}$	$2.7\cdot10^{10}$	3.1	$4.0\cdot10^{8}$	$2.0\cdot10^{8}$	$4.1\cdot10^{-7}$	0.0109	$5\cdot10^{-9}$	$4.93\cdot10^{13}$	0.05

Table 4. Physical constants for all tempers of AA6070.

E (MPa)	ν	ρ (kg/m^3)
70000	0.3	2700

Table 5. Ballistic limit velocities and Recht-Ipson constants from experimental tests and finite element simulations using LS-DYNA and IMPETUS Afea Solver.

Temper	Experimental data			LS-DYNA			Deviation (%)	IMPETUS			Deviation (%)
	a	p	v_{bl} (m/s)	a	p	v_{bl} (m/s)		a	p	v_{bl} (m/s)	
O	1	1.94	348.0	1	2	317.1	-8.9	1	2	315.0	-9.5
T4	1	2.05	506.2	1	2	473.8	-6.4	1	2	470.2	-7.1
T6	1	2.21	562.5	1	2	535.4	-4.8	1	2	530.9	-5.6
T7	1	2.20	529.1	1	2	520.5	-1.6	1	2	515.3	-2.6